

## CONSTRAINTS ON THE PROPERTIES OF THE NEUTRON STAR XTE J1814-338 FROM PULSE SHAPE MODELS

DENIS A. LEAHY<sup>1</sup>, SHARON M. MORSINK<sup>2</sup>, YI-YING CHUNG<sup>3</sup>, & YI CHOU<sup>3</sup>

*Accepted by ApJ: September 26, 2008*

### ABSTRACT

The accretion-powered (non-X-ray burst) pulsations of XTE J1814-338 are modeled to determine neutron star parameters and their uncertainties. The model is a rotating circular hot spot and includes: (1) an isotropic blackbody spectral component; (2) an anisotropic Comptonized spectral component; (3) relativistic time-delays and light-bending; and (4) the oblate shape of the star due to rotation. This model is the simplest possible model that is consistent with the data. The resulting best-fit parameters of the model favor stiff equations of state, as can be seen from the 3- $\sigma$  allowed regions in the mass-radius diagram. We analyzed all data combined from a 23 day period of the 2003 outburst, and separately analyzed data from 2 days of the outburst. The allowed mass-radius regions for both cases only allow equations of state (EOS) that are stiffer than EOS APR (Akmal et al. 1998), consistent with the large mass that has been inferred for the pulsar NGC 6440B (Freire et al. 2008). The stiff EOS inferred by this analysis is not compatible with the soft EOS inferred from a similar analysis of SAX J1808.

*Subject headings:* stars: neutron — stars: rotation — X-rays: binaries — relativity — pulsars: individual: XTE J1814-338

### 1. INTRODUCTION

The accretion-powered millisecond-period X-ray pulsars are promising targets for constraining the neutron star equation of state (EOS) through the modeling of emission from hot spots on the pulsar's surface. The first pulsar discovered in this class, SAX J1808.4-3658 (Wijnands & van der Klis 1998), has a spectrum consistent (Gierliński et al. 2002) with emission from a hot spot on the star's surface. Pulse shape modeling of rapidly rotating neutron stars relies on two relativistic effects: the gravitational bending of light rays reduces the modulation of the pulsed emission and depends on the mass to radius ratio  $M/R$ ; and the Doppler boosting due to the star's rotation creates an asymmetry in the pulse shape and depends on the star's radius  $R$ . These features, combined with reasonable models of the emission properties at the neutron star's surface can be used to constrain the neutron star's mass and radius and hence the EOS of supra-nuclear density matter.

XTE J1814-338 (hereafter XTE J1814) was discovered during outburst in June 2003 (Markwardt & Swank 2003), and is an accretion powered millisecond pulsar with spin frequency 314.36 Hz and orbital period of 4.3 hr (Markwardt et al. 2003). A detailed timing analysis for XTE J1814 was performed by Papitto et al. (2007) to obtain accurate values for orbital period, projected semi-major axis, pulse spin frequency and spin down rate. A similar analysis of the pulse arrival times was carried out by Watts & Strohmayer (2006) and Chung (2007), which both included an analysis of phase lags. Soft lags were found in the 2-10 keV energy band, similar to those for SAX J1808-3658 and consistent with an origin in Doppler

boosting of a Comptonized pulse component with a much broader emission pattern than the blackbody component.

Strohmayer et al. (2003) found the same frequency in the X-ray bursts as was found in the persistent emission, but with a lower second harmonic content. Watts et al. (2008) showed that the X-ray burst oscillations are tightly phase-locked with the non-burst pulsations. Bhattacharyya et al. (2005) modeled the oscillations during X-ray bursts with a hot spot model for a spherical star and for 2 equations of state. Using a large grid of models they found an upper limit on compactness  $R_S/R < 0.48$ , with  $R_S$ , the Schwarzschild radius.

There are pulse shape models for a few other X-ray pulsars. The 1.2 s period X-ray pulsar Her X-1 was modeled by Leahy (2004) using a model that includes accretion columns. The model for Her X-1 constrains the neutron star EOS to a fairly moderate stiffness (Leahy 2004). Zavlin & Pavlov (1998) and Bogdanov et al. (2007) have modeled the X-ray emission from the 5.8 ms period radio pulsar PSR J0437-4715 using a Hydrogen atmosphere model. In the case of PSR J0437-4715, Bogdanov et al. (2007) found that a simple isotropic blackbody model is inconsistent with the data. In their models, Bogdanov et al. (2007) showed that the radius of PSR J0437-4715 must be larger than 6.7 km if the mass is  $1.4M_\odot$ . Unfortunately the mass of this pulsar is not well-constrained. Bogdanov et al. (2008) have shown that constraints on radius for a number of other ms radio pulsars are also possible.

Constraints on SAX J1808.4-3658 (with a spin period of 2.5 ms) were made by Poutanen & Gierliński (2003) using data from the 1998 outburst. The modeling done by Poutanen & Gierliński (2003) included blackbody emission from a hot spot that is Compton scattered by electrons above the hot spot. Their model makes use of a spherical model for the star's surface and does not include the effects of relative time-delays caused by the different time of flights for photons emitted from different

<sup>1</sup> Department of Physics and Astronomy, University of Calgary, Calgary AB, T2N 1N4, Canada; leahy@ucalgary.ca

<sup>2</sup> Department of Physics, University of Alberta, Edmonton, AB, T6G 2G7, Canada; morsink@phys.ualberta.ca

<sup>3</sup> Graduate Institute of Astronomy, National Central University, Jhongli 32001, Taiwan; yichou@astro.ncu.edu.tw

parts of the star’s surface. More recently Cadeau et al. (2005) and Cadeau et al. (2007) have shown that time-delays and the star’s oblate shape are important factors that can affect the outcome of pulse-shape modeling for rapidly rotating pulsars such as SAX J1808.4-3658. The 1998 outburst data for SAX J1808.4-3658 was revisited using a models that included time-delays and oblateness (Leahy et al. 2008) with the result that the EOS for SAX J1808.4-3658 is constrained to be very soft.

In this paper we model the accretion-powered pulsations of XTE J1814 using a hot-spot model. The hot-spot model allows for one or two circular hot spots with a two-component spectrum. The spectral model includes isotropic blackbody emission and an anisotropic Compton-scattered component described by a power-law. The photons are propagated to the observer using the oblate Schwarzschild approximation (Morsink et al. 2007) which allows the photon initial conditions to be placed on an oblate-shaped initial surface determined by an empirical formula. The Schwarzschild metric is used to compute the photon bending angles and time delays since it has been shown (Cadeau et al. 2007) that the corrections induced by the Kerr black hole metric or a numerical metric for a rotating star are insignificant compared to the corrections induced by the oblate shape. In order to do the pulse-shape modeling, we construct light curves in two narrow energy bands, 2-3 keV and 7-9 keV. We first analyse a composite pulse-shape constructed from 23 days of data and then consider pulse-shapes constructed from single days of data in order to determine whether variations of the pulse-shape with time are significant.

The outline of this paper is as follows. In Section 2 the method used to construct the light curves and analyse them is outlined. The results of the best-fit models are presented in Section 3. A discussion of the results is presented in Section 4.

## 2. METHOD

### 2.1. Construction of Light Curves

Pulse shapes for the accretion-powered pulsations are constructed using the ephemeris given by Chung (2007). Data is limited to the first 23 days of the 2003 outburst, June 5 to June 27 2003 (MJD 2452795-2452817), in order to avoid the later period of the outburst when the flux and pulse shape became more erratic (see for example, Watts et al. (2005)). X-ray bursts were cut out of the data during the interval between 100 s before and after the start of each burst.

Although the RXTE observations include data in the range of 2 - 50 keV, we have chosen to concentrate on the lower energy range from 2 - 10 keV for two reasons. First, the data is noisier at energies above 10 keV. Second, the Chandra observations by Krauss et al. (2005) constrain the spectrum in the 2 - 10 keV range. It is also useful to separate the data into narrow energy bands in order to separate the different spectral components. We have chosen two narrow bands, the 2-3 keV band and the 7-9 keV band based on the Chandra spectrum. The narrow-band pulse shapes constructed using data from the full observation period (June 5 - 27) are shown in Figure 1.

We have also investigated the variability of the pulse shape with time. In order to do this, the data was separated into one-day segments and separate light curves

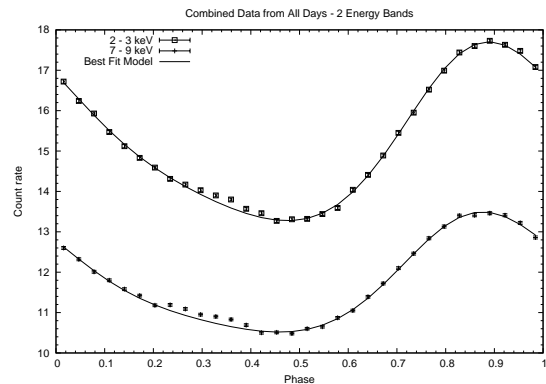


FIG. 1.— Pulse profiles for XTE J1814 constructed with data from all days between June 5 - 27 (excluding X-ray bursts). Light curves for two energy bands, 2-3 keV and 7-9 keV are shown.

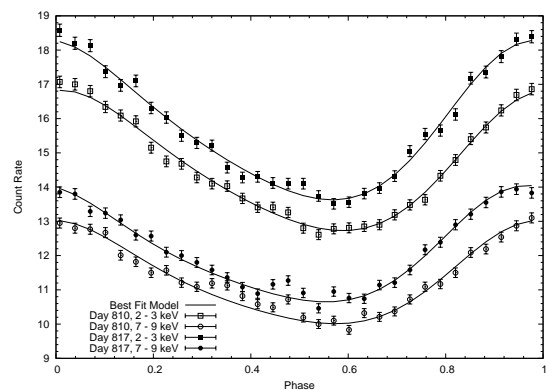


FIG. 2.— One-day pulse profiles for XTE J1814 constructed with data from days June 20 and June 27 (MJD 2452810 and 2452817). Two energy bands are shown for each day.

constructed for each day. It is not computationally feasible to model all days simultaneously, so we instead focus on two separate days. The days were chosen by comparing light curves in the 2 - 10 keV range for different days using a  $\chi^2$  test and selecting two days which differ the most from each other. This also has the effect of selecting days with intrinsically smaller error bars. The days resulting from this selection process correspond to June 20 and 27. Light curves for these two days, in the two narrow energy bands are shown in Figure 2.

### 2.2. Analysis of Light Curves

Krauss et al. (2005) observed XTE J1814 with Chandra on June 20, 2003. They modeled the spectrum in the 0.5 - 10 keV range and found that the best fit solution corresponds to a combination of a 0.95 keV blackbody and powerlaw emission with a photon spectral index of  $\Gamma = 1.4$ . The ratio of flux from the blackbody to the powerlaw in their model is about 10%. We use the Krauss et al. (2005) spectral model and assume that it holds for the other days covered by the RXTE data. This assumption is motivated by the fact that the relative normalization of different energy bands is approximately constant from day to day, although the overall flux at all wavelengths changes with time.

The spectral model of Krauss et al. (2005) motivates the use of two narrow bands in our pulse shape models. A low energy band is necessary in order to capture the blackbody component, so we choose the lowest possible

XTE energy band at 2 - 3 keV. The spectrum in this band is dominated by the powerlaw component, but the blackbody contribution is still important. We also choose the 7 - 9 keV band as the highest energy band covered by the Chandra observation. In this high energy band the blackbody flux is negligible.

Our method for modeling the observed emission is very similar to the method presented in Leahy et al. (2008). The spectral model has three components: (1) Comptonized flux in the high energy band (7-9 keV); (2) Comptonized flux in the low energy band (2-3 keV); and (3) blackbody flux in the low energy band. The observed flux for the  $i$ th component,  $F_i$ , integrated over the appropriate observed energy band is given by

$$F_i(E) = I_i \eta^{3+\Gamma_i} (1 - a_i \mu). \quad (1)$$

In equation (1),  $I_i$  is a constant amplitude,  $\eta$  is the Doppler boost factor,  $\Gamma_i$  is the photon spectral index in the star's rest frame,  $\mu$  is the cosine of the angle between the normal to the star's surface and the initial photon direction, and the constant  $a_i$  describes the anisotropy of the emitted light. For a definition of  $\eta$  as well as a more complete description of the modeling method, please see Leahy et al. (2008).

In our modeling, the amplitudes  $I_1$  and  $I_2$  are free parameters while the third amplitude  $I_3$  is defined through the constant  $b = \bar{F}_3/\bar{F}_2$ , the ratio of the phase-averaged blackbody to Comptonized flux in the low-energy band. In the spectral model by Krauss et al. (2005),  $b = 0.1$ , but we include this parameter as a fitting parameter with  $1\sigma$  limits from their spectral model. The photon spectral indices for the Comptonized components are fixed at  $\Gamma_1 = \Gamma_2 = 1.4$  as given by their model. In the narrow range of the low-energy band the blackbody component of 0.95 keV can be modeled by a powerlaw with photon spectral index  $\Gamma_3 = 0.85$ . The anisotropy parameters for the Comptonized components  $a_1 = a_2 = a$  are assumed to be equal, and the parameter  $a$  is kept as a free parameter.

In the modelling of the non-accreting ms pulsars, it was found (Zavlin & Pavlov 1998; Bogdanov et al. 2007, 2008) that a limb-darkened Hydrogen atmosphere spectral model is required by the data. It is reasonable to expect that the blackbody component of the spectrum should also be limb-darkened. We tested this hypothesis by multiplying the blackbody flux by a limb-darkening function of the form  $e^{-\tau/\mu}$ . We then computed the bestfit neutron star models for two type of models: (1) models with non-zero optical depth  $\tau$  and (2) models with zero optical depth. The bestfit models for these two cases are almost identical: the mass and radius of the bestfit model changes by less than 0.5% when a nonzero optical depth is added, and the value of  $\delta\chi^2 = 0.1$  when the limb-darkening is added. Since the change in  $\chi^2$  and the physical parameters are negligible we conclude that adding an extra parameter to model limb-darkening is not warranted by the data. The reason for this is due to the Chandra model which restricts the blackbody contribution in the 2-3 keV band to only 10% of the Comptonized contribution, and effectively sets the blackbody component to zero in the high energy band. Since the Comptonized flux is dominant and has fan-beaming included, small changes to the anisotropy of the blackbody component don't affect the final models. For this reason

we have set the anisotropy parameter for the blackbody component to zero ( $a_3 = 0$ ). This is consistent with the results found for SAX J1808.4-3658 (Leahy et al. 2008) which also did not require any limb-darkening. The final set of free parameters describing the spectrum are  $I_1$ ,  $I_2$ ,  $b$  and  $a$ .

In order to fit a set of light curves we also need to introduce a set of parameters describing the star and the emission geometry. These parameters are the mass  $M$  and equatorial radius  $R$  of the star, the co-latitude of the spot  $\theta$ , the inclination angle  $i$  as well as a free phase  $\phi$ . The radius of the circular spot (in the star's rest frame) is kept fixed at 1.5 km, as given by the Chandra spectral model (Krauss et al. 2005).

Our models make use of light curves for two different days' data, which requires a separate set of parameters for each day. However, on the two different days the parameters  $M$ ,  $R$  and  $i$  do not change. In order to simplify the analysis, we also assume that the photon spectral indices and the parameters  $a$  and  $b$  are also fixed. The full set of free parameters are:  $\{I_1, I_2, \theta, \phi\}$  for each day plus  $M$ ,  $R$ ,  $i$ ,  $a$  and  $b$ , for a total of 13 free parameters. However, for each of our fits, the ratio  $M/R$  is kept fixed, so for any one value of  $M/R$ , there are only 12 free parameters.

We use the oblate Schwarzschild approximation (Morsink et al. 2007) to connect photons emitted at the star's surface with those detected by the observer. In previous studies (Cadeau et al. 2005, 2007) we have shown that, to the accuracy required for extracting the parameters of a rapidly rotating neutron star, it is sufficient to use the Schwarzschild metric to compute the bending of light rays and the relative time delays of photons emitted at different locations on the star. The extra time delays and light bending caused by frame-dragging or higher order rotational corrections in the metric are negligible. However, the rotation of the star causes a deformation of the star into an oblate shape, which changes (relative to a sphere) the directions that photons can be emitted into. We have developed a simple approximation (Morsink et al. 2007) that allows an empirical fit to the oblate shape of a rotating star to be embedded in the Schwarzschild metric and make use of it in this analysis.

### 3. RESULTS

#### 3.1. Evidence for a Second Spot

The pulse profiles in Figure 1 show a feature in the phase interval between 0.24 and 0.4. This feature is seen in all of the other energy bands as well. In order to investigate the nature of this feature, we restrict the analysis here to just the 7-9 keV light curve. Since the blackbody contribution in this energy band is negligible, we use a simplified model which only includes the Comptonized component of the radiation.

The simplest model for the emission is a single spot. We fitted the 7-9 keV light curve shown in Figure 3 with a single spot model by first fixing  $2M/R = 0.4$  and varying the parameters  $M, i, \theta, a, I$  and  $\phi$ . (Similar results are obtained for other values of  $2M/R$ .) Since there are 32 data points this corresponds to 25 degrees of freedom. The best fit solution for a single spot model has  $\chi^2 = 50.7$ , which is not a very good fit. This best-fit solution is shown as a solid curve in Figure 3.

We now turn to a two-spot model, where the second

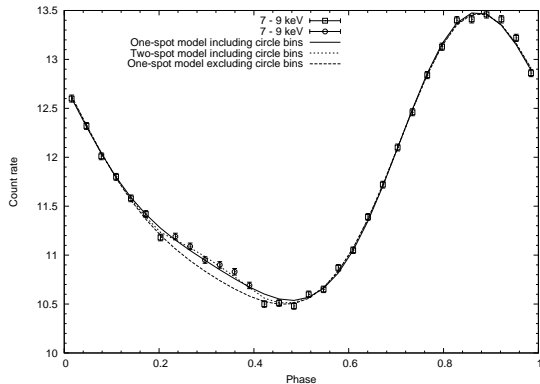


FIG. 3.— Models used to fit the data in the 7-9 keV band (data combined from all 23 days). A one-spot model that uses all data points (both squares and circles) results in the best fit solid curve with  $\chi^2/\text{dof} = 50.7/25$ . A two-spot model that uses all data points results in the best fit dotted curve with  $\chi^2/\text{dof} = 28.3/23$ . A one-spot model that omits the circle bins results in the best fit dashed curve with  $\chi^2/\text{dof} = 19.2/19$ .

spot is allowed to have an arbitrary location relative to the first spot, but the spectrum is assumed to be the same. The introduction of a second spot introduces three new parameters to the model: an intensity and two angles. The resulting fit for  $2M/R = 0.4$  has  $\chi^2 = 28.3$  for 23 degrees of freedom, which is a significant improvement. The light curve for this model is shown with a dotted curve in Figure 3. The mass for this model is  $2.04 M_\odot$ . In this model, the second spot’s location is situated so that the second spot is almost never seen and its light only contributes during the phase interval between 0.24 and 0.4. Outside of this interval the light received only originates from the primary spot. This suggests a simpler one-spot model where bins in the phase interval 0.24 to 0.4 (marked with a circle in Figure 3) are removed from the data set. This reduces the degrees of freedom to 19 (32-6 data points and 5 parameters for a one-spot model). The resulting best-fit model for  $2M/R = 0.4$  has  $\chi^2 = 19.2$ , which is also a significant improvement from the one-spot model that uses all of the data. The mass for this model is  $2.08 M_\odot$  and the light curve for this model is shown as a dashed line in Figure 3.

Comparing the two-spot model with the one-spot model with the circle-bins excluded, we see that the difference in  $\chi^2$  is not significant, and there is little change between the best-fit values of mass and radius. This leads us to the conclusion that there is good evidence for a second spot (or a feature that mimics a second spot), but that the amount of data encoded in those bins affected by the second spot is not sufficient to allow us to model the details of the second spot with any confidence. Since the inclusion or exclusion of the second spot does not change the best-fit values of the main physical parameters of the star ( $M, R, i$ ) it is more appropriate to choose the simpler one-spot model. The qualitative results do not change when we look at different energy bands. As a result, for the remaining modeling reported in this paper we only use one-spot models where data in the 0.24 - 0.4 phase range is removed from the analysis.

### 3.2. Best-fit Models using Data from All Days

Our procedure for modeling the two-energy band data shown in Figure 1 is to assume a one-spot model that includes both blackbody and Comptonized emission. Data

TABLE 1  
COMPARISON OF THE TWO MINIMA.

| Model     | $2M/R$ | $M$<br>$M_\odot$ | $R$<br>km | $\theta$<br>deg. | $i$<br>deg. | $a$  | $M_c$<br>$M_\odot$ | $\chi^2/\text{dof}$ |
|-----------|--------|------------------|-----------|------------------|-------------|------|--------------------|---------------------|
| High Mass | 0.3    | 2.86             | 28.7      | 66.8             | 11.8        | 0.81 | 1.70               | 55.9/42             |
| Low Mass  | 0.3    | 1.95             | 19.8      | 42.4             | 25.0        | 0.59 | 0.55               | 61.0/42             |

in the phase period between 0.24 and 0.4 is omitted, as described in section 3.1. We do a number of fits, each with a fixed value of  $2M/R$ . (Fixing the ratio of  $M/R$  simplifies the fitting procedure since the light-bending and time delays depend on this ratio.) Once  $2M/R$  is fixed, all other parameters are allowed to vary and the minimum value of  $\chi^2$  is found. In addition to the parameters described in Section 2.2, we also added two parameters corresponding to DC offsets for the two energy bands. This allows for small errors in the background subtraction. Once  $2M/R$  is fixed, we have a total of 10 free parameters:  $M, \theta, i, a, b$ , 2 amplitudes, 2 DC offsets and one overall phase. (The parameter  $b$  is restricted to have a value that is within  $1 \sigma$  of the value found by Krauss et al. (2005).) Since each energy band has 32 points, but we exclude 6 of these points we have  $64 - 12 - 10 = 42$  degrees of freedom.

For a fixed value of  $2M/R$ , we find that there are two local minima. These two minima are shown in Table 1 and we label these two best-fit solutions as the high and low mass solutions. The lowest value of  $\chi^2$  corresponds to the high mass solution and the lower mass solution has a higher value of  $\chi^2$ . Although the high mass solution is a better fit, we exclude this solution on physical grounds. First of all, it requires a neutron star radius of 28 km, which is not allowed by any known equation of state. Secondly, once the neutron star mass and the inclination angle are known, the companion’s mass can be calculated (shown in the column labeled  $M_c$  in Table 1). In the high mass case the companion’s mass is  $1.7 M_\odot$ . Due to the dim nature of the companion, Krauss et al. (2005) have shown that the companion (if a main sequence star) would have to have a mass that is no bigger than  $0.5 M_\odot$ . Clearly this excludes the high mass solution but allows the lower mass solution. For these reasons, we exclude the high mass solutions.

In Table 2 the best-fit solution for each value of  $2M/R$  is shown. In each case only the lower mass solution is shown. The best-fit solution shown as a solid curve in Figure 1 corresponds to the  $2M/R = 0.4$  solution shown in the Table 2. Although we call this these solutions “lower mass”, clearly they still correspond to high mass neutron stars. In Table 2, only solutions for  $2M/R = 0.3$  to 0.6 are shown. In the case of less compact stars, such as  $2M/R = 0.2$ , the only solution corresponded to the “high mass” branch of unphysical solutions. We did not test solutions that were more compact than  $2M/R = 0.6$  since these solutions would allow spots to have multiple images, and our program is unable to handle multiple images. Technically, the solutions with  $2M/R = 0.6$  could have spots with multiple images, but we have checked that the relative values of  $\theta$  and  $i$  do not lead to this problem for our solutions for the most compact stars.

In Figure 4 we show a number of mass-radius curves for stars spinning at 314 Hz as well as the 2- and 3-

TABLE 2  
BEST-FIT SOLUTIONS USING DATA FROM ALL DAYS.

| $2M/R$ | $M$<br>$M_{\odot}$ | $R$<br>km | $\theta$<br>deg. | $i$<br>deg. | $a$  | $M_c$<br>$M_{\odot}$ | $\chi^2/\text{dof}$ |
|--------|--------------------|-----------|------------------|-------------|------|----------------------|---------------------|
| 0.3    | 1.95               | 19.8      | 42.4             | 25.0        | 0.59 | 0.55                 | 61.0/42             |
| 0.4    | 2.45               | 18.4      | 47.0             | 24.2        | 0.61 | 0.65                 | 61.2/42             |
| 0.5    | 2.38               | 14.2      | 36.7             | 39.4        | 0.59 | 0.39                 | 61.9/42             |
| 0.6    | 2.42               | 11.9      | 40.9             | 42.8        | 0.59 | 0.37                 | 62.6/42             |

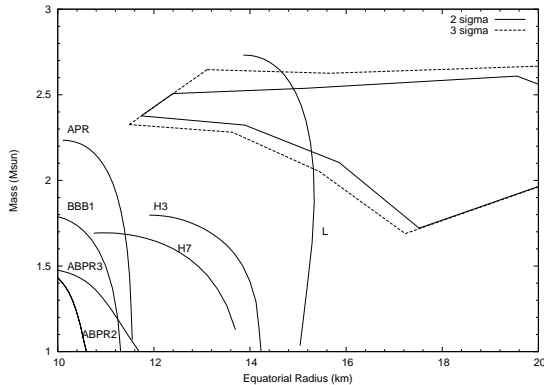


FIG. 4.— Best-fit mass and radius values using the combined data from all days, separated into two narrow energy bands. Contours shown are for 2- and 3- $\sigma$  confidence levels. Mass-Radius curves for stars spinning at 314 Hz are shown as solid curves. The EOS shown are: APR (Akmal et al. 1998), BBB1 (Baldo et al. 1997), ABPR2-3 (Alford et al. 2005), H3-7 Lackey, Nayyar, & Owen (2006) and L (mean-field theory, pure neutrons (Pandharipande et al. 1976)).

$\sigma$  confidence regions for the “low mass” solutions. (In this figure, the radius  $R$  refers to the equatorial radius.) These regions are found by fixing the value of  $2M/R$ , and varying all other parameters and finding the solutions that have  $\chi^2$  larger than the global minimum of  $\chi_{min}^2 = 61.0$  by  $\delta\chi^2 = 4$  ( $2\sigma$ ) or 9 ( $3\sigma$ ). The region allowed with 99.7% confidence ( $3\sigma$ ) only includes large stars with high mass. Of the equations of state displayed in Figure 4, the only one lying in the  $3\sigma$  allowed region is L, corresponding to pure neutron matter computed in a mean field approximation (Pandharipande et al. 1976). A pure neutron core is unlikely to be the correct description of supra-nuclear density matter. However it is possible for an EOS that includes some softening due to the presence of other species to be allowed by this data.

### 3.3. Best-fit Models Using Data From 2 Days

It is possible for variability of the data to affect the fit results, as appears to be the case for SAX J1808 (Leahy et al. 2008). For this reason we have rebinned the data into one-day segments in order to see if there is any significant change in the pulse shape on a day to day basis. We performed a  $\chi^2$  test to see how closely each day’s data matched the other days’ data. Comparisons of one day with an adjacent day gave values of  $\chi^2/\text{dof}$  ranging from 0.8 to 1.6, indicating day-to-day changes are small. The largest change is between day 810 (June 20) and day 817 (June 27) with  $\chi^2/\text{dof} = 4.8$ . Light curves in the two narrow energy bands for these two days are shown in Figure 2.

The data corresponding to these two days is binned into 32 bins per period. Since we continue to remove the 6 bins corresponding to the second “spot”, this corre-

TABLE 3  
BEST-FIT SOLUTIONS USING DATA ONLY FROM DAYS 810 & 817.

| $2M/R$ | $M$<br>$M_{\odot}$ | $R$<br>km | $\theta_1$<br>deg. | $\theta_2$<br>deg. | $i$<br>deg. | $a$  | $M_c$<br>$M_{\odot}$ | $\chi^2/\text{dof}$ |
|--------|--------------------|-----------|--------------------|--------------------|-------------|------|----------------------|---------------------|
| 0.2    | 1.18               | 18.4      | 33.6               | 34.7               | 33.8        | 0.55 | 0.29                 | 123.9/92            |
| 0.3    | 1.71               | 17.3      | 34.1               | 35.3               | 32.0        | 0.55 | 0.39                 | 124.6/92            |
| 0.4    | 2.13               | 16.1      | 35.1               | 36.6               | 33.6        | 0.55 | 0.43                 | 125.4/92            |
| 0.5    | 2.41               | 14.4      | 37.1               | 38.7               | 36.3        | 0.55 | 0.43                 | 127.5/92            |
| 0.6    | 2.55               | 12.6      | 39.5               | 41.4               | 39.9        | 0.56 | 0.41                 | 132.0/92            |

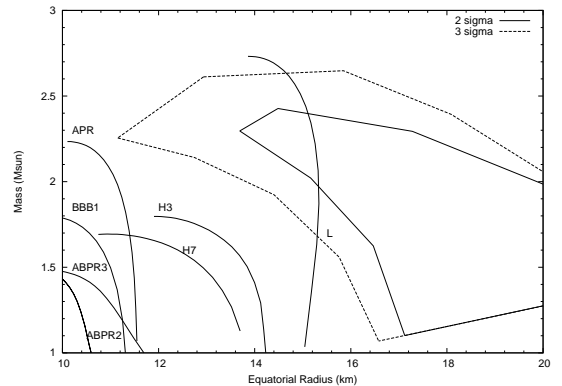


FIG. 5.— Best-fit mass and radius values using data only from day 810 and 817, separated into two narrow energy bands. Contours shown are for 2- and 3- $\sigma$  confidence levels. EOS labels are the same as in Figure 4.

sponds to a total of 104 data points. We fit the data for these two days by assuming that the parameters  $M, R, i, a$  are the same for both days. The spot’s latitude is allowed to vary, as are the amplitudes of the energy bands and the value of phase. Since the DC contributions found in our previous fits are very small, we do not include terms for DC offsets. In addition, we keep the value of  $b$  fixed at the Krauss et al. (2005) value in order to simplify the fits. This corresponds to 12 parameters, and a total of 92 degrees of freedom.

The best-fit solutions for this 2-day joint fit are shown in Table 3. For each fixed value of  $2M/R$  we only found one minimum, unlike the case with all days included. The angular locations of the spot on the two days are labeled  $\theta_1$  and  $\theta_2$ . The change in angular location of the spot between the two days is less than  $2^\circ$  in all cases. The solutions continue to have large masses and radii, as in the case of fits using all of the data. In the case of  $2M/R = 0.2$  a low mass ( $1.2 M_{\odot}$ ) solution is allowed, but it has a very large radius. The 2- and 3- $\sigma$  confidence regions for the two-day joint fits are shown in Figure 5. The 3- $\sigma$  confidence region is somewhat larger than the same region computed using all of the data, but the two methods have a significant overlap. The 2-day joint fit also only allows the stiffest EOS L.

### 3.4. Dependence of Models on Assumed Parameters

The models in this paper depend on the results of the spectral models of Krauss et al. (2005). We now consider the effect of allowing the parameters in the spectral model to vary within the error bars. As mentioned in Section 2.2 we already allow the ratio of the blackbody to powerlaw components ( $b$ ) to vary within the  $1\sigma$  limits given by the Krauss et al. (2005) spectral model.

Another spectral parameter that could affect the fits is the photon spectral index  $\Gamma$  for the powerlaw component of the spectrum. Krauss et al. (2005) found a value of  $\Gamma = 1.41 \pm 0.06$  and in all of our models presented in the previous section we kept the photon spectral index fixed at a value of  $\Gamma = 1.40$ . We would expect that a larger value of  $\Gamma$  would allow for smaller stars. This is because the flux in Equation (1) is proportional to the Doppler boost factor  $\eta$  raised to the power  $\Gamma + 3$ . The Doppler boost factor is mainly responsible for introducing higher harmonics into the signal, so a larger value of  $\Gamma$  creates a more asymmetric pulse shape. In order to compensate, the best-fit solution will require a smaller value of stellar radius  $R$  in order to decrease the value of  $\eta$ . In order to test the dependence of the best-fit values of the parameters on  $\Gamma$ , we chose a value of  $\Gamma = 1.50$  which is somewhat larger than the range allowed by Krauss et al. (2005) and fit the data using the same method described earlier in this paper. The results of the best-fit parameters for the two values of  $\Gamma$  for the case of  $2M/R = 0.4$  are shown in Table 4. As expected, increasing  $\Gamma$  allowed for a smaller star, but the decrease is only by 3%. Similar results occur for other values of  $M/R$ . Clearly the dependence on the photon spectral index is not sensitive enough to affect the resulting large size of the best-fit stars.

In our models we keep the spot size (as measured on the star’s surface) fixed at a diameter of 3 km. In previous modeling (Leahy et al. 2008) of SAX J1808.4-3658 we found that the final values of the best-fit parameters were not sensitive to changes in the spot size, assuming that the spot is small compared to the size of the star. For this reason we have kept the spot size fixed at 3 km for all models in this analysis. We have also assumed the hot spot is circular, although recent MHD models (Kulkarni & Romanova 2005) more complicated spot shapes. In this paper we have only attempted to use the simplest possible model that is still consistent with the data. Adding extra parameters to our models in order to describe more complicated spot shapes is not yet warranted by the quality of the data.

For all models computed so far, we have made use of an empirical formula for the oblate shape of the star, and have included the relative time-delays for photons emitted from different parts of the star. In Table 4 the effects of oblateness and time-delays on the fits are shown. For the model labeled “sphere”, a spherical initial surface was assumed, but relative time-delays were included in the computation. The resulting best-fit solution is about 10% larger than the corresponding oblate model (labeled “oblate” and  $\Gamma = 1.4$  in Table 4). This shrinkage of the star’s radius when oblateness is included has been observed in the modeling of SAX J1808.4-3658 (Leahy et al. 2008). For the model labeled “no td” time-delays were omitted from the calculation and a spherical surface was used. Comparison of the two spherical models in Table 4 shows that the model that includes time-delays is about 3% smaller than the model that omits time-delays.

### 3.5. Comparison with X-ray Burst Data

In our analysis of XTE J1814 we have only included data from the accretion-powered pulsations and have omitted any data corresponding to an X-ray burst.

TABLE 4  
DEPENDENCE OF MODELS ON PARAMETERS. JOINT FITS FOR TWO ENERGY BANDS FOR TWO SEPARATE DAYS (810 AND 817).

| Model  | $\Gamma$ | $\frac{2M}{R}$ | $M$<br>$M_{\odot}$ | $R$<br>km | $\theta_1$<br>deg. | $\theta_2$<br>deg. | $i$<br>deg. | $a$  | $M_c$<br>$M_{\odot}$ | $\chi^2/\text{dof}$ |
|--------|----------|----------------|--------------------|-----------|--------------------|--------------------|-------------|------|----------------------|---------------------|
| oblate | 1.4      | 0.4            | 2.13               | 16.1      | 35.1               | 36.6               | 33.6        | 0.55 | 0.43                 | 125.4/92            |
| oblate | 1.5      | 0.4            | 2.07               | 15.6      | 34.5               | 35.9               | 34.3        | 0.55 | 0.41                 | 126.6/92            |
| sphere | 1.4      | 0.4            | 2.38               | 17.6      | 32.8               | 34.3               | 31.6        | 0.54 | 0.49                 | 124.7/92            |
| no td  | 1.4      | 0.4            | 2.45               | 18.5      | 49.0               | 50.9               | 21.1        | 0.60 | 0.76                 | 126.8/92            |

Bhattacharyya et al. (2005) analyzed the light curves constructed from the X-ray bursts for this neutron star. In their analysis they assumed a spherical surface for the star and traced the paths of the X-rays using the Kerr metric. They also made use of a limb-darkened blackbody emission (2 keV) spectral model appropriate for X-ray bursts. Due to the method that they adopted, it was necessary for them to assume one of two different equations of state. The stiffer EOS used by Bhattacharyya et al. (2005) is the same as the EOS that we label “APR” and is the A18+ $\delta v$ +UIX computed by Akmal et al. (1998). The analysis of the X-ray bursts by Bhattacharyya et al. (2005) allows the APR EOS, while our analysis of the accretion-powered pulsations only allows stiffer EOS. From their analysis it is difficult to determine whether or not their analysis of the X-ray burst data is consistent with a very stiff EOS, as indicated by our analysis.

Watts et al. (2005) provide a detailed analysis of many aspects of both the X-ray bursts and the non-burst emission. One of the quantities that they measured was the fractional amplitude of the pulsations at the fundamental frequency and the first harmonic for both the burst and non-burst emission. They found that the non-burst emission (modeled in this paper) has a larger harmonic content than the burst emission studied by Bhattacharyya et al. (2005). Since Doppler boosting is partially responsible for the harmonic content, it is perhaps not surprising that our analysis of the non-burst pulsations implies a larger Doppler factor for the star, which in turn implies a larger radius than a similar analysis for the X-ray burst oscillations.

## 4. DISCUSSION

We have analyzed the accretion-powered (non-X-ray burst) pulsations of XTE J1814 using a hot spot model. Our modeling includes (1) an isotropic blackbody spectral component; (2) an anisotropic Comptonized component; (3) relativistic time-delays; (4) the oblate shape of the star due to rotation. The model presented in this paper is the simplest possible model that is consistent with the data. The resulting best-fit models favor stiff equations of state, as can be seen from the 3- $\sigma$  allowed regions in Figures 4 and 5. In Figure 4 all data from a 23 day period of the 2003 outburst were included, while for Figure 5 data from only 2 days were included. The allowed regions for the two data sets differ slightly, but both only allow equations of state that are stiffer than EOS APR (Akmal et al. 1998).

It is interesting that a large mass has been inferred for the pulsar NGC 6440B (Freire et al. 2008) through measurements of periastron precession. Assuming that the observed periastron precession is purely from rela-

tivistic effects, the pulsar's mass is  $M = 2.74 \pm 0.21 M_{\odot}$  ( $1\text{-}\sigma$  error bars) (Freire et al. 2008). If the mass really is this high, it would be consistent with the stiff equations of state allowed by our analysis of XTE J1814. However, it is still possible that the large periastron precession observed for NGC 6440B could be caused by a very rapidly rotating companion Freire et al. (2008), in which case the pulsar's mass would be smaller and compatible with more moderate equations of state. A high mass for SAX J1808.4-3658 is also inferred by observations during its quiescent state (Heinke et al. 2007). Modelling of the neutron star X7 in 47 Tuc (Heinke et al. 2006) allows for a high mass neutron star, although for X7 a low mass neutron star is also allowed.

Similar hot spot models of SAX J1808.4-3658 imply a soft equation of state and a column model for Her X-1 also implies a soft EOS (see Leahy et al. (2008) and Leahy (2004) for details). The best-fit pulse-shape models found for XTE J1814 have mass and radius incompatible with the  $3\text{-}\sigma$  allowed regions of mass and radius found for SAX J1808.4-3658 or Her X-1. Some possible interpretations could be (1) time-variations in the pulse profile of SAX J1808.4-3658 led to an underestimate of the star's radius; (2) the equation of state for dense matter has a two-phase nature allowing both large and small compact stars; or (3) the simple hot-spot model doesn't describe one or more of these pulsars.

The first reason is a factor for SAX J1808.4-3658. It was demonstrated in Leahy et al. (2008) that the analysis of the pulse profile averaged over a long observation gave significantly different results than the pulse profile obtained from a much shorter observation. Supporting this conclusion is a recent analysis by Hartman et al. (2008) of data from the 1998, 2002 and 2005 outbursts of SAX J1808.4-3658 showing a great deal of variation in the pulse shape over time (see Figure 3 of Hartman et al. (2008)). The pulse-shape analysis by Leahy et al. (2008) only made use of the data from the 1998 outburst. The 1998 data is very sinusoidal in nature and has very little harmonic content. The results of Hartman et al. (2008) show that the later outbursts have a stronger harmonic content. Since a larger radius star can produce a stronger harmonic content, it is possible that the addition of data from 2002 and 2005 will alter the conclusions of Leahy et al. (2008) about SAX J1808. But the effect of pulse shape variability is not a factor for Her X-1 where the pulse shape has high stability.

The second reason above, i.e. a bimodal equation of state, is a possible, but speculative, solution to the greatly different allowed regions for M and R. In this scenario, there is still only one baryonic equation of state and one quark matter EOS, but above a certain critical density,  $\rho_{crit}$ , the whole star makes a transition from baryonic matter to quark matter. Then for stars with central density  $\rho_c$  having  $\rho_c < \rho_{crit}$ , the M vs. R relation follows a stiff baryonic EOS, somewhat like EOS L, whereas for  $\rho_c > \rho_{crit}$  the star has converted to a quark star and lies on a quark matter EOS curve in the mass-radius diagram. In the case of EOS L, the  $3\sigma$  region with  $M < 2.7 M_{\odot}$  would require a value of  $\rho_{crit} \sim 10^{15} \text{g/cm}^3$ . Since quark matter EOS curves have a lower maximum mass than baryonic EOS curves, any baryonic star that makes the transition and has mass above the quark star maximum mass must lose mass to end up as a stable quark star. The mass loss depends on the physics of the transition process and is likely vary from star to star. In this scenario, we interpret XTE J1814 to lie on the baryonic branch of the mass vs. radius diagram and SAX J1808.4-3658 and Her X-1 to lie on the quark matter branch.

The third listed reason for the discrepancy, that the emission region models are too simple to represent the actual emission regions on the stars, is a definite possibility. For instance, if the emission is coming from the magnetosphere, then our models are incorrect. Alternatively, the emission may arise from surface spots, but the region's shape might be more complicated than a circle. This can only be tested by constructing more complex models and applying them to the observed pulse shapes. However with a more complex model with more parameters describing the model, better pulse shape data is required to constrain the model parameters. Future work is planned to explore more complex emission models, and to test whether these resolve the apparent discrepancy in mass and radius for different pulsars.

This research was supported by grants from NSERC to D. Leahy and S. Morsink. Y. Chung and Y. Chou acknowledge partial support from Taiwan National Science Council grant NSC 95-2112-M-008-026-MY2. We also thank the Theoretical Physics Institute at the University of Alberta for supporting D. Leahy's visits to the University of Alberta.

#### REFERENCES

- Akmal, A., Pandharipande, V. R., & Ravenhall, D. G. 1998, Phys. Rev. C, 58, 1804
- Alford, M., Braby, M., Paris, M., & Reddy, S. 2005, ApJ 629, 969
- Baldo, M., Bombaci, I., & Burgio, G. F., 1997, A&A, 328, 274
- Bhattacharyya, S., Strohmayer, T. E., Miller, M. C., & Markwardt, C. B. 2005, ApJ, 619, 483
- Bogdanov, S., Rybicki, G. B., & Grindlay, J. E. 2007, ApJ, 670, 668
- Bogdanov, S., Grindlay, J. E., & Rybicki, G. B. 2008, ArXiv e-prints, 801, arXiv:0801.4030
- Cadeau, C., Leahy, D. A., & Morsink, S. M. 2005, ApJ, 618, 451
- Cadeau, C., Morsink, S. M., Leahy, D. A., & Campbell, S. S. 2007, ApJ, 654, 458
- Chung, Y. 2007, Study of Orbital and Pulsation Properties of Accretion-Powered Millisecond Pulsar XTE J1814-338, MSc. Thesis, National Central University, Taiwan.
- Freire, P. C. C., et al. 2008, ApJ, 675, 670
- Gierliński, M., Done, C., & Barret, D. 2002, MNRAS, 331, 141
- Hartman, J. M., et al. 2008, ApJ, 675, 1468
- Heinke, C. O., Rybicki, G. B., Narayan, R., & Grindlay, J. E. 2006, ApJ, 644, 1090
- Heinke, C. O., Jonker, P. G., Wijnands, R., & Taam, R. E. 2007, ApJ, 660, 1424
- Krauss, M. I., et al. 2005, ApJ, 627, 910
- Kulkarni, A. K. & Romanova, M. M. 2005, ApJ, 633, 349
- Lackey, B. D., Nayyar, M., & Owen, B. J. 2006, Phys. Rev. D, 73, 024021
- Leahy, D. A. 2004, ApJ, 613, 517
- Leahy, D. A., Morsink, S. M., & Cadeau, C. 2008, ApJ, 672, 1119
- Markwardt, C. B., & Swank, J. H. 2003, IAU Circ., 8144, 1
- Markwardt, C. B., Strohmayer, T. E., & Swank, J. H. 2003, Astron. Telegram, 164, 1
- Morsink, S. M., Leahy, D. A., Cadeau, C. & Braga, J. 2007, ApJ, 663, 1244
- Pandharipande, V. R., Pines, D., & Smith, R. A. 1976, ApJ, 208, 550

- Papitto, A., di Salvo, T., Burderi, L., Menna, M. T., Lavagetto, G., & Riggio, A. 2007, MNRAS, 375, 971
- Pechenick, K. R., Ftaclas, C., & Cohen, J. M. 1983, ApJ, 274, 846
- Poutanen, J. & Gierliński, M. 2003, MNRAS, 343, 1301
- Strohmayer, T. E., Markwardt, C. B., Swank, J. H., & in't Zand, J. 2003, ApJ, 596, L67
- Sunyaev, R. A., & Titarchuk, L. G. 1985, A&A, 143, 374
- Watts, A. L., Strohmayer, T. E., & Markwardt, C. B. 2005, ApJ, 634, 547
- Watts, A. L., & Strohmayer, T. E. 2006, MNRAS, 373, 769
- Watts, A. L., Patruno, A., & van der Klis, M. 2008, ArXiv e-prints, 805, arXiv:0805.4610
- Wijnands, R., & van der Klis, M. 1998, Nature, 394, 344
- Zavlin, V. E., & Pavlov, G. G. 1998, A&A, 329, 583